Asociación Argentina de Astronomía
Third La Plata International School on Astronomy and Geophysics:
Chaos, diffusion and non–integrability in Hamiltonian Systems
Applications to Astronomy , 2012
P. M. Cincotta, C. M. Giordano & C. Efthymiopoulos, eds.

LECTURE

Diffusion in multidimensional Hamiltonian Systems Application to Galactic Dynamics

P.M. Cincotta [1,2], C.M. Giordano[1,2]

(1) Instituto de Astrofísica de La Plata (CONICET)
(2) Grupo de Caos en Sistemas Hamiltonianos
Facultad de Ciencias Astronómicas y Geofísicas - UNLP
Paseo del Bosque, B1900FWA La Plata, Argentina

Abstract. In the present lectures we provide results and discussions concerning the processes that lead to local and global chaotic diffusion in phase space of multidimensional conservative systems. We investigate and provide a measure of the extent of the domain over which diffusion may occur. All these issues are thoroughly discussed by dealing with a toy model such as the perturbed quartic oscillator as well as with a multidimensional conservative map that would be representative of the dynamics of a resonance interaction, which is an important mechanism in several astronomical systems, like the Solar System or galaxies.
Most of the contents of the present lectures are based on previous works of the authors already published in several journals.

1. Introduction

An open issue in multidimensional Hamiltonian systems is the so–called *chaotic diffusion*, that is, those mechanisms under which either global or local actions of an integrable Hamiltonian change over phase space (or action space) under the effect of a non–integrable perturbation. This kind of phenomena arises in Solar System and planetary dynamics, stellar dynamics such as star clusters and galaxies as well as in many other dynamical problems, like chemical reactions or particle acellerators.

At the present any complete theory that could describe global instabilities in phase space of multidimensional systems is still lacking. One could acquire accurate values of several indicators of the stability of the motion, but they would only provide local information for a neighborhood of a some point of phase space. A given orbit in a chaotic component in, for instance a 3D potential could have, positive and large values of two of its Lyapunov exponents, which does not necessarily mean that the unperturbed integrals will vary over vast domains.

Even though near–integrable Hamiltonian systems have been largely investigated –perhaps starting with the study conducted by Poincaré in the late nineteenth century (Poincaré 1893)–, the problem has not been completely elucidated yet. In fact, questions such as the stability of the motion of high–dimensional systems are far from being thoroughly understood. Some progress on transport phenomena has been made during the last two decades, but almost all the at-

tained results concern only low-dimensional symplectic maps or in other cases, non conservative one-dimensional maps, and it appears rather difficult to extent these approaches to be applied to many-dimensional Hamiltonians or conservative maps. Moreover, it is unclear how these approaches provide information about the role played by the torus structure and their invariant manifolds in spreading or preventing diffusion in phase space (see for instance, Meiss 1992, Venegerolies 2008, Korabel & Klags 2004).

Developing further in this direction Chirikov (1979) pioneered a complete survey of this matter in a somewhat heuristic way by using a standard mathematical language. Following this improvement, Cincotta (2002) revisited Chirikov's arguments, particularly that related to the so–called Arnol'd diffusion.

Regarded as a global instability, Arnol'd diffusion appears to be closer to a theoretical conjecture rather than to a real physical process (see Arnol'd 1964; Chirikov & Vecheslavov 1989; Chirikov & Vecheslavov 1993; Chirikov *et al.* 1985; Cincotta 2002). In fact, there remain so many unsolved mathematical details that Arnol'd diffusion, as a global instability, results a rather controversial question (see Lochak 1999). Further, the more recent numerical evidence reveals that Arnol'd diffusion might operate in certain (somewhat artificial) dynamical systems (Guzzo *et al.* 2005, 2006; Lega *et al.* 2010). In fact, in a previous work Lega *et al.* (2008), investigated diffusion in near–integrable Hamiltonian Systems (or symplectic maps) and discuss and compute local and global Arnol'd diffusion in two different scenarios, the Froeschlé four-dimensional map (see Froeschlé 1971, 1972) and a 3D Hamiltonian model previously investigated by for instance Guzzo *et al.* (2002), Froeschlé *et al.* (2005). Also in the lecture by Efthymiopoulos (2012) in this proceedings, a thoroughly discussion about Arnol'd diffusion (or diffusion along a singe and/or double resonance) is presented, using the same 3D Hamiltonian system mentioned above, including rather instructive pictures of how diffusion proceeds. Besides an attempt to relate the size of the remainder of the optimal normal form construction and Chirikov's Arnol'd diffusion coefficient estimate is discussed. We strongly recommend the interested reader to explore in the exhaustive list of references on the subject in this mentioned lecture.

Nonetheless, it has been shown that Arnol'd diffusion–like processes may play a significant role in global chaotic diffusion in phase space, (Giordano & Cincotta 2004); (Cachucho *et al.* 2010), though the mechanisms that drive the diffusion remain still unknown. By *Arnol'd diffusion–like* we mean, chaotic transport along resonance (or relics of resonances), that geometrically resembles Arnol'd diffusion, but in those scenarios most of the phase space is chaotic, mainly due to strong overlap of the main resonances so the systems is quite far from the regime under which Arnol'd diffusion is usually investigated. Roughly speaking, the perturbation is not small enough such that most of the resonance structure is preserved (see the discussions given in the present lecture).

In (Cachucho *et al.* 2010) Chirikov's diffusion approach is applied to the (5,-2,-2) three body mean motion resonance for the (490) Verita's family. It is shown that the theoretical arguments used by Chirikov to describe Arnol'd diffusion could also apply in this realistic problem in which the so–called guiding resonance domain is completely chaotic. However, the scenario of modulational

diffusion (Chirikov *at al.* 1985) could perhaps be more suitable to describe the large diffusion observed in the eccentricity of asteroids.

In the present lecture we discuss a preliminary study of diffusion on phase space for a rather simple dynamical system in order to elucidate its efficiency to connect different chaotic components, already given in Giordano & Cincotta (2004) and Giordano & Cincotta (2008). Despite the simplicity of the adopted model, several results concerning its dynamics apply to any 3D Hamiltonian system exhibiting a divided phase space, such as galactic or planetary systems. In Section 4., two values for the perturbation parameter have been selected so that the dynamics of the toy model Hamiltonian resembles that of a galactic system (for a moderate perturbation, in which case both components are comparable) and asteroidal dynamics (for a large perturbation for which the chaotic component prevails).

Observational evidence, theoretical arguments and N-body simulations suggest that a model resembling an isolated elliptical galaxy should exhibit a divided phase space and therefore the perturbation should be moderate (see, for instance Merritt & Friedman 1996; Merritt & Valluri 1996, Papaphilippou & Laskar 1998; Gerhard & Binney 1985; Poon & Merritt 2002; Muzzio *et al.* 2005).

Herein in Section 5.2. we also show, discuss and measure chaotic diffusion in action space by means of a conservative multidimensional map, the Coupled Rational Shifted Standard Map (CRSSM), whose global dynamical properties have been previously studied in Cincotta *et al.* (2003) –CGS03 hereafter–, for different sets of parameters, by recourse of the Mean Exponential Growth Factor of Nearby Orbits (MEGNO). First introduced by Cincotta & Simó (2000) and latter generalized in CGS03, the MEGNO is a rather efficient indicator of the dynamics belonging to the class of the so–called fast indicators, which has already become of widespread use. Many applications of this tool to Solar System dynamics, exoplanets models and as well as to many other dynamical systems could be found throughout the literature. The obtained results are taken from Cincotta & Giordano (2012).

Furthermore, we provide a simple tool which turns to be suitable for measuring the variation of the unperturbed integrals. We face the difficulty to compute a meaningful diffusion coefficient, due to the fact that, as far as we know, it still remains unclear which would be the appropriate approach to be considered, in particular, how the variance of the variables scales with time. In fact, in case of normal diffusion the variance scales linearly with time, but for what is called abnormal diffusion, the scaling runs like t^b where the parameter b is in general unknown and further, it strongly depends on the local dynamical structure of the deemed region of phase space (see for instance, Cordeiro & Mendes de Souza 2005, Cordeiro 2006, Mestre 2012). The exhaustive numerical exploration performed in Cincotta & Giordano (2012) and the results of their application are discussed in Section 5.5.

2. A real galaxy

A galaxy is a very complex physical system since it is composed of $\sim 10^{11} - 10^{15}$ stars whose space distribution (or density) generates its own gravitational field. Some types of galaxies present a rotating pattern, spiral arms and bars. Gas

and dust are generally present, star formation processes occur, supernova explosions release a large amount of energy and the chemical evolution certainly should affect the hydrodynamics. Besides, galaxies are not isolated: gravitational interaction with other galaxies and stellar clusters is always present. It is claimed that a super–massive black hole lies in the center of any galaxy. Thus, all these processes and interactions should be considered when modeling a rough real galaxy, which in fact seems to be a rather difficult problem to cope with. Further aspects are still open, like for instance if they are in a steady state or how to cope with the unknown dark matter, if actually dark matter does exist (see the lecture by Carati & Galgani 2012 in the present volume).

3. A galaxy as an idealization of a N–particle Hamiltonian system

Following Binney & Tremaine (1987), let $f^{(N)}(\boldsymbol{x}_1, \cdots, \boldsymbol{x}_N, \boldsymbol{p}_1, \cdots, \boldsymbol{p}_N, t)$ be the N–particle probability density or distribution function (DF) on 2N–D phase space Γ, so it satisfies the Liouville theorem:

$$\frac{\mathrm{d}f^{(N)}}{\mathrm{d}t} = 0.$$

Let us define the 1 – particle DF:

$$f^{(1)}(\boldsymbol{x}_1, \boldsymbol{p}_1, t) = \int f^{(N)} \mathrm{d}^3x_2 \cdots \mathrm{d}^3x_N \mathrm{d}^3p_2 \cdots \mathrm{d}^3p_N,$$

Assuming that:

- $|(\boldsymbol{x}_i, \boldsymbol{p}_i)|^k f^{(N)} \to 0$ as $|(\boldsymbol{x}_i, \boldsymbol{p}_i)| \to \infty \quad \forall k, \forall i = 1, \cdots, N,$
- $f^{(N)}$ is symmetric in $\boldsymbol{x}_1, \cdots, \boldsymbol{x}_N; \boldsymbol{p}_1, \cdots, \boldsymbol{p}_N,$
- the 2–particle DF could be written in terms of the 2–particle correlation function:

$$f^{(2)}(\boldsymbol{x}_1, \boldsymbol{p}_1, \boldsymbol{x}_2, \boldsymbol{p}_2, t) = f^{(1)}(\boldsymbol{x}_1, \boldsymbol{p}_1, t)\, f^{(1)}(\boldsymbol{x}_2, \boldsymbol{p}_2, t) + g(\boldsymbol{x}_1, \boldsymbol{p}_1, \boldsymbol{x}_2, \boldsymbol{p}_2, t),$$

- the 2 – particle correlation function $g \approx 0$ (Two–body relaxation time: $T_R \sim 10^{15}$ yrs.),
- $N \gg 1,$
- and $f(\boldsymbol{x}, \boldsymbol{v}, t) \equiv \mathrm{N} f^{(1)}(\boldsymbol{x}_1, \boldsymbol{p}_1/m, t)$
- $(\boldsymbol{x}, \boldsymbol{v}) \equiv (\boldsymbol{x}_1, \boldsymbol{p}_1/m)$

we arrive to the so-called collisionless Boltzmann (or Vlasov) equations:

$$\frac{\partial f}{\partial t} + [f, H] = 0, \quad H(\boldsymbol{p}, \boldsymbol{x}) = \frac{\boldsymbol{p}^2}{2} + \Phi(\boldsymbol{x}, t), \qquad \boldsymbol{p} \equiv \boldsymbol{v},$$

being $\Phi(\boldsymbol{x}, t)$ a smooth potential generated by the star distribution. This is the Liouville theorem in the 6–D phase space, μ. Thus, it is necessary to solve:

$$\frac{\partial f}{\partial t} + \nabla_{\boldsymbol{x}} f \cdot \boldsymbol{v} - \nabla_{\boldsymbol{x}} \Phi \cdot \nabla_{\boldsymbol{v}} f = 0,$$

and the Poisson equation:

$$\nabla^2 \Phi = 4\pi G m \int f(\boldsymbol{x}, \boldsymbol{v}, t) \mathrm{d}^3 v.$$

3.1. Steady state solutions

A steady state solution for the collisionless Boltzmann and Poisson equations is given by the so–called strong Jeans Theorem (Lynden–Bell 1962, Binney & Tremaine 1987):

The DF of a steady–state galaxy in which almost all orbits are regular with incommensurable frequencies may presumed to be a function only of three independent isolating integrals.

An *isolating integral* $I(\boldsymbol{x}(t), \boldsymbol{v}(t)) = c$ defines a manifold in μ of lower dimension than $\dim(\mu)$. In Jeans Theorem, the three isolating integrals are, for instance, the three global actions or integrals of $H(\boldsymbol{p}, \boldsymbol{x})$.

An alternative version of the Jeans Theorem could be stated as follows:

If the Hamiltonian of a collisionless stellar system in steady-state equilibrium is Arnol'd–Liouville integrable, the DF has a constant value at every point in an invariant torus of the system (Efthymiopoulos et al. 2008).

But galaxies should present a divided phase space. Therefrom the implementation of Jeans theorem in more realistic stellar systems is rather difficult, for instance:

- It is unclear how the approximate integrals or actions should be included as arguments of the DF when the system is near–integrable;
- Resonances and resonance intersections are dense in phase space;
- One or two integrals do not exist for the chaotic domains of phase pace.

A generalization for non–integrable potentials is given by Merritt (1999):

The phase space density of a stationary stellar system must be constant within every well-connected region.

But:

- An invariant non–resonant torus is a well–connected region when $t \to \infty$,
- A resonant elliptic torus also is a well–connected region of lower dimension (2D) and when $t \to \infty$,

- An hyperbolic tours, also has a lower dimension, and the dynamics is much more complicate when we add a non–in tegrable perturbation to an integrable Hamiltonian,
- Are the chaotic domains in phase space well–connected regions?

Therefore it is rather important to investigate chaotic diffusion in phase space to understand, for instance, if a single chaotic component does exist. To deal with this issue we can use a non–integrable Hamiltonian (toy) model or instead a multidimensional map. Thus, we will be considering a perturbed 3D quartic oscillator and a 4D symplectic map.

4. Chaotic diffusion of orbits in systems with a divided phase space for a 3D Hamiltonian system

In order to build up an equilibrium model for a galaxy which is assumed to be represented by a smooth gravitational field it is necessary to know beforehand its global dynamics. It seems likely that any realistic model should exhibit a divided phase space, that is, the motion would take place either in a stable, regular component or in one or more unstable, chaotic components. In 3D systems displaying such a dynamics, the existence of three, in general local, invariants, allows the presence of invariant tori where regular, quasi-periodic or resonant motion takes place. The disruption of these local invariants, mainly due to resonance interactions, leads to the appearance of a chaotic component.

However, the first attempts to investigate these matters in the astrophysical literature assumed that for dynamical systems with more than two degrees of freedom, the chaotic component is fully connected. In fairly recent studies, such as Merritt & Valluri (1996) and Merritt & Fridman (1996), the authors study whether this full connection of the chaotic component may occur in realistic physical times. If such were the case, it would imply that the orbit of a star within the chaotic domain would explore the whole region, which, in general, would comprise a large fraction of the energy surface. As a consequence the distribution function on the chaotic component would depend only on the energy (see Merritt (1999) for a thorough discussion).

As shown in Giordano & Cincotta (2004) we obtained numerical evidence that for moderate-to-strong chaotic systems diffusion does not occur over the whole chaotic component and only when the latter fills almost all the energy surface may diffusion become significant but in extremely large times. We chose a rather simple Hamiltonian system, the perturbed quartic oscillator in order to have a complete knowledge of the local and global dynamics and the transition to chaos, and particularly to be able to study in detail the motion in the resonance intersections. The forthcoming sections summarize the main results of this work.

Therefore, let us now be concerned with the perturbed uncoupled quartic oscillator:

$$\tilde{H}(\boldsymbol{p},\boldsymbol{q}) = \frac{\boldsymbol{p}^2}{2} + \frac{1}{4}(x^4 + y^4 + z^4) + \varepsilon x^2(y+z). \tag{1}$$

whose full dynamics has been investigated by Cincotta & Giordano (2002) and Cincotta *et al.* (2003) by means of the *Mean Exponential Growth factor of*

Nearby Orbits (MEGNO) (a detailed formulation of this technique can be found in Cincotta *et al.*, 2003 and Cincotta & Simó, 2000.)

The advantage of this 3D toy model is that it can be easily written in terms of action variables and that the coordinates admit of a simple Fourier expansion. Indeed, in terms of the unperturbed action-angle variables, $(I_1, I_2, I_3; \theta_1, \theta_2, \theta_3)$, the Hamiltonian (1) can be recast as

$$H(\boldsymbol{I}, \boldsymbol{\theta}) = H_0(\boldsymbol{I}) + \varepsilon V(\boldsymbol{I}, \boldsymbol{\theta}), \tag{2}$$

where

$$H_0(\boldsymbol{I}) = A\left(I_1^{4/3} + I_2^{4/3} + I_3^{4/3}\right), \tag{3}$$

with $A = (3\beta/2\sqrt{2})^{4/3}$, $\beta = \pi/2K(1/\sqrt{2})$, $K(k)$ denoting the complete elliptic integral. The perturbation, which can be assumed to be small as long as $\varepsilon \ll 1$, admits of the Fourier expansion

$$\begin{aligned} V(\boldsymbol{I}, \boldsymbol{\theta}) &= \hat{V}_{12} \sum_{n,m,k=1}^{\infty} \alpha_{nmk} \Big(\cos\left(2(n+m-1)\theta_1 \pm (2k-1)\theta_2\right) \\ &+ \cos\left(2(n-m)\theta_1 \pm (2k-1)\theta_2\right) \Big) \\ &+ \hat{V}_{13} \sum_{n,m,k=1}^{\infty} \alpha_{nmk} \Big(\cos\left(2(n+m-1)\theta_1 \pm (2k-1)\theta_3\right) \\ &+ \cos\left(2(n-m)\theta_1 \pm (2k-1)\theta_3\right) \Big), \end{aligned} \tag{4}$$

the functions $\hat{V}_{ij}$ and the coefficients α_{nmk} being

$$\begin{aligned} \hat{V}_{ij} &= 2^{5/2} 3 \beta^4 I_i^{2/3} I_j^{1/3}, \qquad \alpha_{nmk} = \alpha_n \alpha_m \alpha_k, \\ \alpha_s &= \frac{1}{\cosh\left((s-1/2)\pi\right)}, \qquad \frac{\alpha_{s+1}}{\alpha_s} \approx \frac{1}{23}, \end{aligned}$$

and can be split in two, namely V_{xy} and V_{xz}, on introducing the integer vectors $\boldsymbol{l} = (l_1, l_2, 0)$ and $\boldsymbol{k} = (k_1, 0, k_3)$, and the new coefficients $\hat{\alpha}_{l_1 l_2}$ and $\hat{\alpha}_{k_1 k_3}$,

$$\begin{aligned} V_{xy}(I_1, I_2; \theta_1, \theta_2) &= \hat{V}_{12} \sum_{l_1, l_2} \hat{\alpha}_{l_1 l_2} \cos(l_1 \theta_1 + l_2 \theta_2), \\ V_{xz}(I_1, I_3; \theta_1, \theta_3) &= \hat{V}_{13} \sum_{k_1, k_3} \hat{\alpha}_{k_1 k_3} \cos(k_1 \theta_1 + k_3 \theta_3). \end{aligned}$$

The concomitant unperturbed frequency vector is given by

$$\boldsymbol{\omega}(\boldsymbol{I}) = \frac{\partial H_0}{\partial \boldsymbol{I}} = \frac{4}{3} A \left(I_1^{1/3}, I_2^{1/3}, I_3^{1/3}\right). \tag{5}$$

The knowledge of the resonance structure of the unperturbed Hamiltonian H_0, is of actual relevance. Here the resonance structure on the energy surface can be easily visualized by introducing a change of coordinates such that

the unperturbed energies in each degree of freedom, h_1, h_2, h_3, become the new action–like variables. We obtain

$$\begin{aligned} H_0(h_1,h_2,h_3) &= h_1+h_2+h_3, \\ \boldsymbol{\omega}(h_1,h_2,h_3) &= \sqrt{2}\beta\big(h_1^{1/4},h_2^{1/4},h_3^{1/4}\big), \end{aligned}$$

and, in terms of (h_1, h_2), the resonance condition, $\boldsymbol{m}\cdot\boldsymbol{\omega}=0$, $\boldsymbol{m}\in\boldsymbol{Z^3}/\{\mathbf{0}\}$, for $H_0 = h$ can be recast in the form

$$\begin{aligned} &(m_1^4+m_3^4)\xi^4+4m_1^3m_2\xi^3\eta+6m_1^2m_2^2\xi^2\eta^2 \\ &+4m_1m_2^3\xi\eta^3+(m_2^4+m_3^4)\eta^4-m_3^4=0, \end{aligned} \tag{6}$$

where $\xi=(h_1/h)^{1/4}$, $\eta=(h_2/h)^{1/4}$.

Note that for those harmonics in which one of the m_i is zero, the resonant polynomial (6) can be easily solved to yield

$$\hat{h}_2 = \frac{m_1^4}{m_2^4}\hat{h}_1, \quad m_1m_2<0, \quad m_3=0, \tag{7a}$$

$$\hat{h}_2 = 1-\Big(\frac{m_1^4+m_3^4}{m_3^4}\Big)\hat{h}_1, \quad m_1m_3<0, \quad m_2=0, \tag{7b}$$

$$\hat{h}_2 = \Big(\frac{m_3^4}{m_2^4+m_3^4}\Big)(1-\hat{h}_1), \quad m_2m_3<0, \quad m_1=0, \tag{7c}$$

with $\hat{h}_i = h_i/h$, showing that those resonances associated to resonant vectors with at least one null m_i appear as straight lines on the energy surface $\hat{h}_1+\hat{h}_2+\hat{h}_3=1$.

The width of any of those resonances can be computed by means of a simple pendulum approximation, which is a suitable description in the case in which we assume each resonance is isolated from the rest.

Let us notice that the map $\mathbf{I}\mapsto\mathbf{h}$ transforms the unperturbed energy surface into a plane, so that we can perform a second (global) change of coordinates, $(h_1,h_2,h_3)\mapsto(e_1,e_2,e_3)$, in such a way that the e_3–axis is normal to the energy plane,

$$e_1 = \frac{1}{\sqrt{6}}(h_1-2h_2+h_3), \tag{8a}$$

$$e_2 = \frac{1}{\sqrt{2}}(h_1-h_3), \tag{8b}$$

$$e_3 = \frac{1}{\sqrt{3}}(h_1+h_2+h_3), \tag{8c}$$

with

$$-\sqrt{\frac{2}{3}}\le\frac{e_1}{h}\le\frac{1}{\sqrt{6}}, \quad -\frac{1}{\sqrt{2}}\le\frac{e_2}{h}\le\frac{1}{\sqrt{2}}, \quad \frac{e_3}{h}=\frac{1}{\sqrt{3}}. \tag{9}$$

The resonance structure of the unperturbed system on the energy surface and the theoretical widths of the principal resonances appearing in the perturbation are presented in Figs. 1[a] and [b], respectively.

On applying the MEGNO to the study of the global dynamics of Eq. (1), one obtains the resonance structure presented in Fig. 1[c]. There, the details of the phase space structure at a low-to-moderate value of the perturbation ($\varepsilon = 5 \times 10^{-3}$) are displayed, depicting the obtained values for the MEGNO in a contour–like plot where resonances can be clearly distinguished.

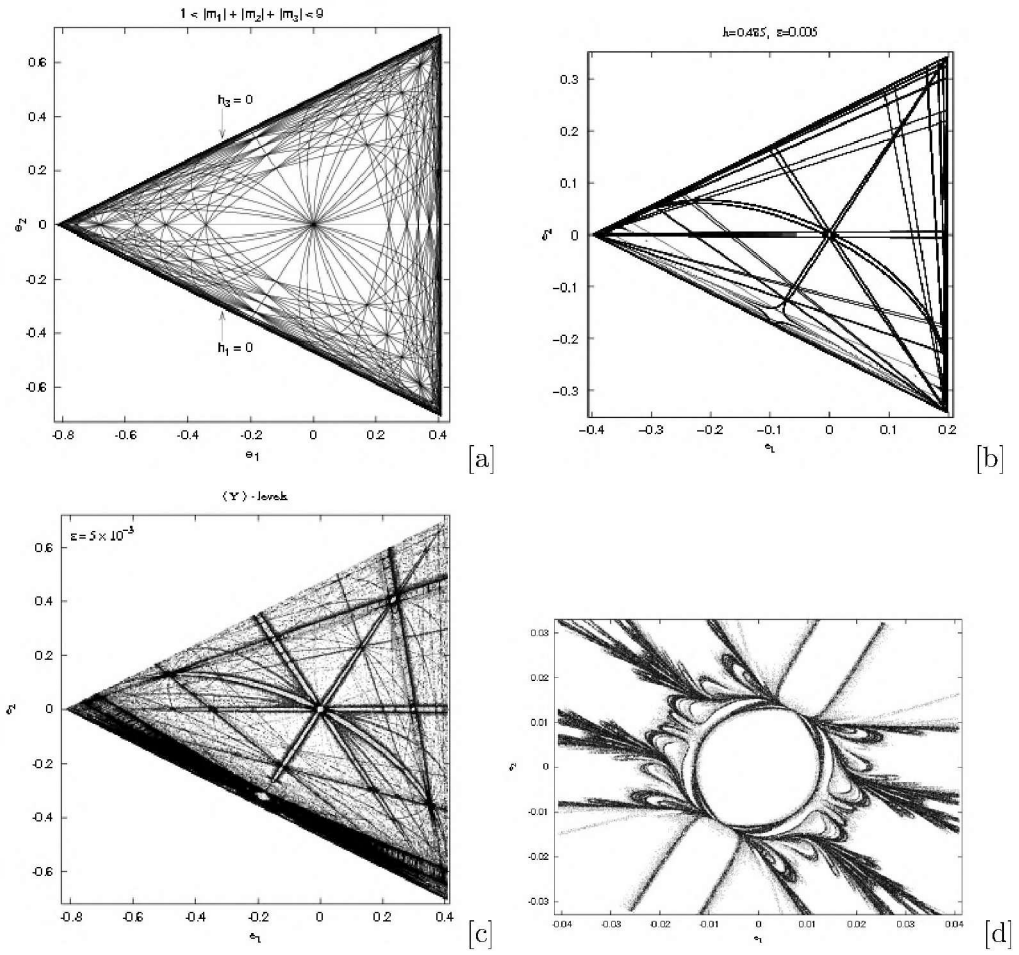

Figure 1. [a] Resonances of the unperturbed Hamiltonian (3) for $1 < |m_1| + |m_2| + |m_3| < 9$ for the rescaled energy $h = 1$ yielding the theoretical Arnold web on the energy surface. [b] Strongest resonances and their theoretical widths for $\varepsilon = 0.005$. [c] Actual dynamics of the system revealed by the MEGNO for the same value of ε. [d] Blow up around the origin. These figures were taken from Cincotta *et. al*, 2003 and Mestre *et. al*, 2009.

At this stage, a brief reference to MEGNO's behavior is required in order to grasp the dynamical information comprised in such a figure. Let us then recall that in the case of regular motion, the MEGNO ($\overline{Y}$) tends asymptotically to a fixed value independent of the orbit, namely $\overline{Y} \to 2$. Small departures

from this value indicate the proximity of some periodic orbit, where $\overline{Y} \lesssim 2$ and $\overline{Y} \gtrsim 2$ for stable and unstable periodic orbits, respectively. On the other hand, for irregular, stochastic motion $\overline{Y}$ grows linearly with time as $t \to \infty$, at a rate equal to $\sigma/2$, σ denoting the largest Lyapunov Characteristic Number (LCN) of the orbit.

Let us devote the following paragraphs to describe the procedure giving rise to Fig. 1[c], and Figs. 2, which correspond to higher values of the perturbation.

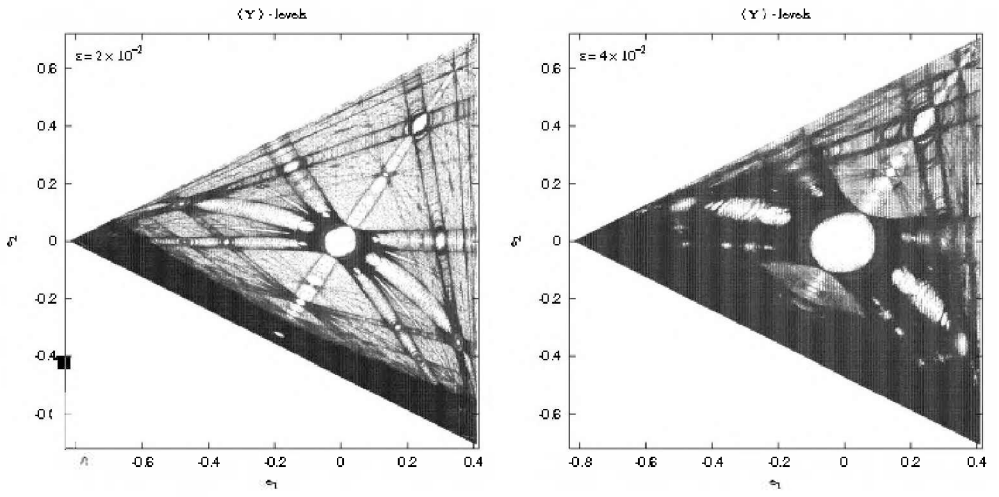

Figure 2. $\overline{Y}(t_f)$–levels on the energy surface for $\varepsilon = 0.02$ and 0.04.

For each adopted value of ε, we take values of h_1 and h_2 with $0 \le h_1, h_2 \le h$, $h_3 = h - h_1 - h_2$, where h_1 and h_2 are of the form $jh/1,000$; $j = 0, \ldots, 1,000$. This leads to 501,501 initial conditions for which we take $(x, y, z) = (0, 0, 0)$. The equations of motion are integrated together with their first variationals over a total motion time $t_f = 3,500T$. For the tangent vector, we adopt the initial values $\delta_x = \delta_y = \delta_z = 0$ and δ_{p_i} chosen at random in the interval $(-1, 1)$ and then normalized to 1. For each orbit we compute both $\overline{Y}(t_f)$ and the rate at which the MEGNO grows with time. The actual energies h_1, h_2, h_3, are scaled to the interval $[0, 1]$ (by division through h) and then transformed to the energy plane (e_1, e_2) by means of Eqs. (8).

In Fig. 1[c], corresponding to $\varepsilon = 5 \times 10^{-3}$, we display the values of $\overline{Y}(t_f)$ binned in five intervals, two of them being very narrow and close to 2 (see figure caption for details).

In this picture most of the main resonances can be clearly distinguished as light gray channels surrounded by dark boundaries. Four main resonances are seen to intersect at the origin: the three lines corresponding to the $(1, -1, 0)$, $(1, 0, -1)$, $(0, 1, -1)$ resonances and the curve associated to the $(-2, 1, 1)$ resonance.

The actual width of the resonances as well as the narrow stochastic layers at their edges can be clearly visualized. The center of any resonance "channel" corresponds to a sequence of 2D elliptic tori while its borders ("stochastic layer") correspond to a sequence of 2D hyperbolic tori. We observe a strip of chaotic

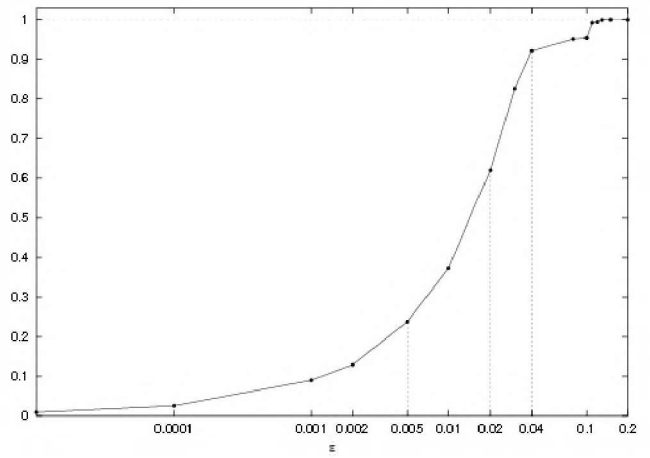

Figure 3. Fraction of chaotic motion vs. ε (in logarithmic scale). The vertical lines refer to the values of ε adopted for Fig. 1[c] and Fig. 2.

motion close to $h_1 = 0$. The presence of this region is easily understood from Fig. 1a as the overlap of the strongest resonances, e.g. $(2, -1, 0)$ and $(2, 0, -1)$, as well as of many others (not shown in Fig. 1[a]).

The dynamics at the intersection of resonances can be quite intricate. To illustrate such a feature, let us note the complexity of the picture reproduced in Fig. 1[d], where we present a zoom around the intersection of resonances at the origin in Fig. 1[c]. That contour plot was obtained with a higher resolution in h_1 and h_2 and for a total motion time $t_f = 350T$. There the MEGNO reveals the existence of several stability zones, which should be responsible for restraining the spread of chaotic motion, acting as barriers to diffusion. They are the well-known sticky tori surrounding the periodic orbit located at the center of the resonance. This plot is also very illustrative to see how the manifolds of lower dimensional tori bend in a complex fashion, giving rise to the many tight loops seen in the picture. These manifolds are important because they are the objects able to carry the motion arriving along one of the resonances either to the "other part" of the resonance or to a different resonance.

As the perturbation is increased, resonances become wider. Fig. 2 displays the actual structure of action space ($\boldsymbol{e}$–space) for two different (rather large) values of the perturbation parameter, namely $\varepsilon = 0.02$ and $\varepsilon = 0.04$. There, some details of the dynamics at moderate-to-high-level perturbations are shown in a plot similar to that in Fig. 1[c]. The character of the motion (resonant, quasi-periodic and stochastic) is represented in gray scale, from white to black, the different $\overline{Y}(t_f)$ intervals have been selected so as to sharpen the details of the phase space structure in each case.

Notice that for $\varepsilon = 0.02$ a significant part of the energy surface still looks regular, with wide resonance domains and a broad chaotic strip, while it looks rather chaotic for a somewhat slightly larger perturbation. Note however that within the weaker chaotic region, the MEGNO is still capable of unveiling the relics of resonance structures.

In Fig. 3 we present the fraction of chaotic motion as ε is increased, fixing a threshold of $\overline{Y}(t_f) = 2$ below which orbits are regarded as regular. The global amount of stochasticity as a function of ε is measured by counting how many pixels have a value of $\overline{Y}$ that exceeds the adopted threshold. The fraction of chaotic motion for the values of ε considered above, namely 0.02 and 0.04, are 38% and 91.7%, respectively. Further, for values of $\varepsilon \geq 0.1$ the system exhibits completely chaotic dynamics.

4.1. Diffusion on the energy surface at moderate–to–high perturbation

Let us now analyze the diffusion on energy surface at moderate–to–high perturbations, following several orbits with initial conditions in different stochastic domains.

Table 1. Initial conditions on the energy surface for seven orbits with high values of the MEGNO. The energies h_1, h_2 are given in units of $h/250$, where $h = 1/(4\beta^4)$ is the total energy. The exact values of e_1 and e_2 should be obtained by means of Eqs. (8); their approximated values have been included so that they can be easily visualized on the energy surfaces.

i.c.	h_1	h_2	e_1	e_2
i	20	100	−0.0816	−0.3112
ii	10	125	−0.2041	−0.2969
iii	85	69	0.1143	−0.0565
iv	58	21	0.3053	−0.3116
v	70	134	−0.2482	0.0678
vii	104	140	−0.2776	0.2771
vii	191	15	0.3347	0.4157

For seven different initial conditions listed in Table 1 we have followed the wandering of the unperturbed integrals over the (e_1, e_2)-plane. We have picked two initial conditions in the chaotic strip close to $h_1 = 0$, (i) and (ii) –see Fig. 2, another in the region surrounding the more regular central zone at the origin (iii) and four other initial conditions located near the crossing of resonances $(iv) - (vii)$; all of them have very high values of the MEGNO. The origin has also been considered; it actually corresponds to a regular orbit.

The equations of motion have been integrated by means of a Runge–Kutta 7/8th order integrator (the so-called Dopri8 routine, see Hairer *et al*, 1987).

The results corresponding to $\varepsilon = 0.02$ for a total motion time of 3×10^6 characteristic periods T of the system are presented in Fig. 4[a] (we refer to the corresponding Fig. 2 for comparison). We note that even in the case of moderate perturbation, diffusion is completely irrelevant over such a timescale. Only when the resonances labelled by the harmonics $(2, -1, 0)$ and $(2, 0, -1)$ overlap does fast diffusion occur along such resonances, but it is restricted to a relatively small region of the energy surface. For the remaining initial conditions considered the unperturbed integrals remain confined to rather small domains. In particular,

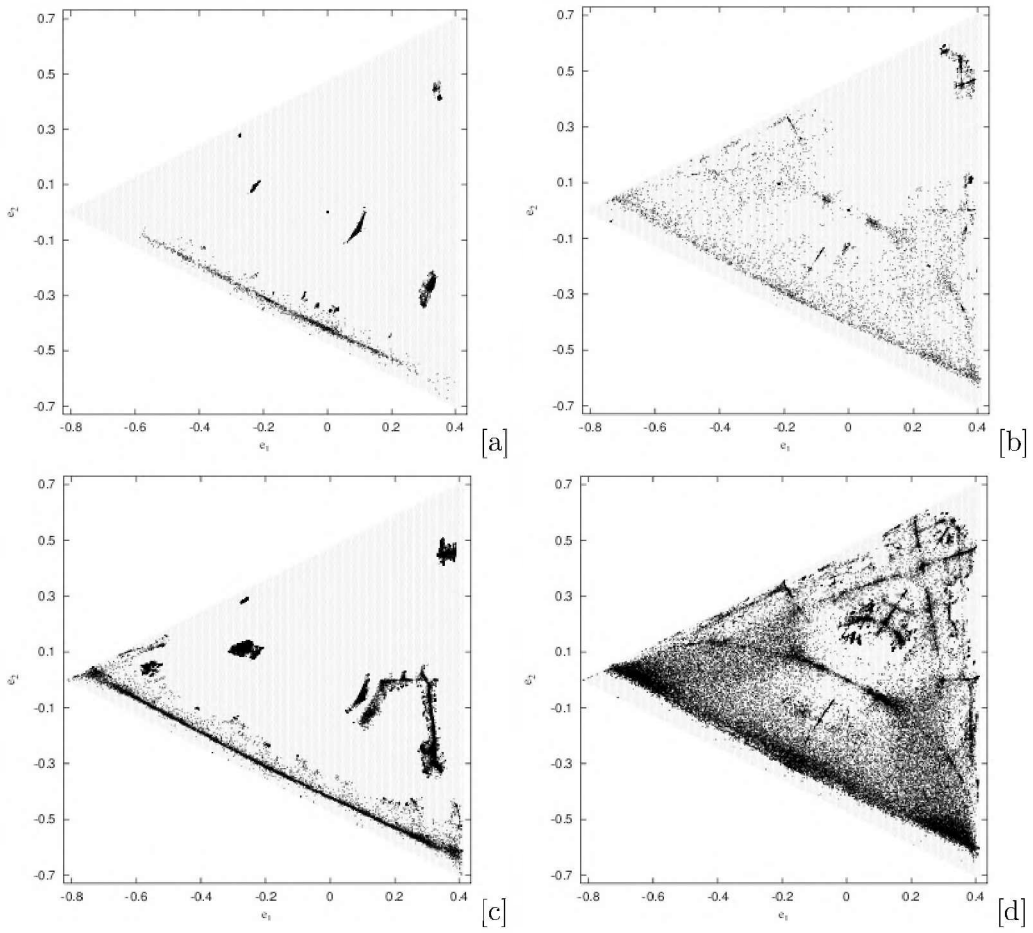

Figure 4. Diffusion on the energy surface at moderate–to–high perturbations after 3×10^6 characteristic periods T of the system for: [a] $\varepsilon = 0.02$, and [b] $\varepsilon = 0.04$; and after $3 \times 10^8 T$ for: [c] $\varepsilon = 0.02$, and [d] $\varepsilon = 0.04$.

for the initial condition (vi) selected near the boundary $h_3 = 0$, the variation of the unperturbed integrals proves to be small, differing slightly from the expected behavior in case of stability. For the regular orbit at the origin, considered just for illustrative purposes, the wandering is restrained to a point, as expected.

The plot in Fig. 4[b] corresponds to $\varepsilon = 0.04$ and should be compared with the contour plot in Fig. 2, where the chaotic regime prevails. Notice must be taken however that in the central region in the latter figure, for which $t_f = 3,500T$, there lie several chaotic orbits; the light gray points and even some of the white points within it have values of the MEGNO larger than 2 (as indicated in the caption). Recall that for constructing Fig. 2 the values of the MEGNO are binned in intervals chosen so as to highlight the dynamical structure of phase space, rather than discriminate stable quasiperiodic motion from chaotic motion. Thus, those chaotic orbits depicted in white in the contour plot having MEGNO values smaller than 2.1 are likely to behave in a regular fashion for rather short timescales, such as $3,500T$. Furthermore, Fig. 3 reveals that for $\varepsilon = 0.04$,

the system shows up as globally chaotic, with just a small fraction of phase space occupied by stable motion. This explains why, for the larger total motion time now considered, 3×10^6 characteristic periods T of the system, diffusion manages to trespass the central zone, the points being mainly concentrated along a fairly well–defined strip corresponding to the curve associated to the $(-2, 1, 1)$ resonance (see below). Note that the upper part of the central zone remains unvisited at this timescale, except for a rather strong but confined concentration of points near the corner.

On considering an even larger timescale, 3×10^8 characteristic periods T of the system, for $\varepsilon = 0.02$ (Fig. 4[c]) the fast diffusion occurring at the overlap of the resonances $(2, -1, 0)$ and $(2, 0, -1)$ after 3×10^6 periods now spreads and continues upwards along the resonances near the borders $h_3 = 0$ and $h_2 = 0$. For the initial condition (vi) chosen at a resonance crossing near $h_2 = 0$, the variation of the unperturbed integrals that was restrained to a small domain in Fig. 4[a] for the lower timescale, now moves upwards, then proceeds to the right and finally goes downwards, the path being drawn by three different resonances. Notice, however, that on this timescale the wandering does not reach the banana-shaped domain on the right corresponding to the initial condition (iii), probably due to the complexity of the dynamics at resonance intersections (recall how intricate such crossings may be). Summing up, on this timescale and for $\varepsilon = 0.02$ the unperturbed integrals still roam over unconnected restraint zones of the energy surface. There remain very localized diffusion domains and the chaotic component seems far from being fully connected.

Instead, for $\varepsilon = 0.04$, after 3×10^8 characteristic periods T of the system the chaotic component is seen to be almost fully connected through the relics of the resonance structure (Fig. 4[d]). The upper right part of the energy surface, formerly empty, now appears densely populated by concentrations mainly along some still distinguishable remaining resonances.

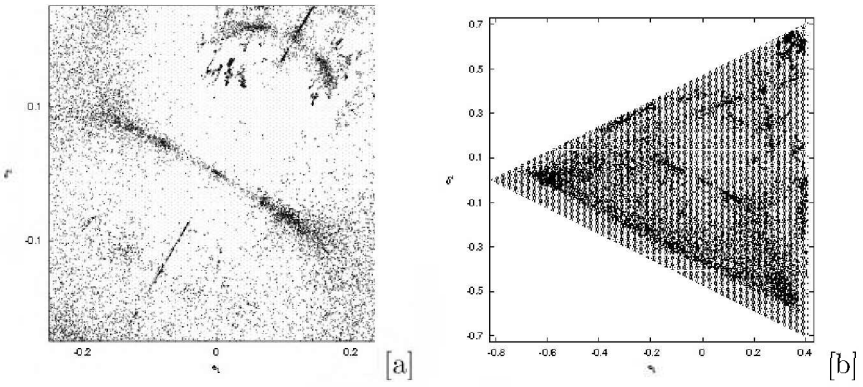

Figure 5. [a] Enlargement of Fig. 4[d] around $(e_1, e_2) = (0, 0)$. [b] Diffusion of a single orbit over the energy surface for $\varepsilon = 0.04$ and $t_f = 6 \times 10^8\ T$ (see text for details).

Fig. 5[a] displays an enlargement of the central region in Fig. 4[d], to see whether any unvisited domain still remains in that part of the energy surface for such a large timescale. A strong concentration of points persists along the strip

already present in Fig. 4[b] for 3×10^6 periods, namely, the curve associated to the $(-2, 1, 1)$ resonance.

In view of the results obtained for $\varepsilon = 0.04$ on the larger timescale, we integrate a single orbit, the initial condition (i) taken in the chaotic strip near the border $h_1 = 0$, for an even larger t_f, 6×10^8 characteristic periods T, and trace the path of its unperturbed integrals over the energy surface, with the aim of verifying whether this path covers the whole chaotic component. The results are displayed in Fig. 5[b], and should be compared with the plot in Fig. 4[d] for seven different initial conditions in Table 1 corresponding to chaotic orbits. As seen in the picture, for this single orbit the unperturbed integrals trail over the chaotic component, the relics of resonances serving as routes. It should be mentioned that, for half the total motion time considered, the upper part of the energy surface remained yet unreached, and it took a much longer time to visit the whole chaotic component.

5. Diffusion in multidimensional maps

In this section we present the results concerning the investigation of chaotic diffusion in discrete dynamical systems, most of which were already published in Cincotta & Giordano (2012).

5.1. The Mean Exponential Growth Factor of Nearby Orbits (MEGNO) for maps

For our exploring the action space of a multidimensional map, we wield the generalized MEGNO, for discrete dynamical systems.

The generalized version of the MEGNO, along with its implementation to discrete dynamical systems, which is in order for the current applications, are given also in CGS03. Though, just for the sake of completeness permit us to provide a brief description of how this tool should be applied in the latter case.

For a given map P, the initial point Q_0 is iterated to yield the points $Q_k = P^k(Q_0)$, while the differential map DP transports an initial "random" tangent vector, v_0, $\|\mathrm{v}_0\| = 1$, providing vectors $\mathrm{v_k} = \mathrm{DP^k(Q_0)v_0}$. Then, after N iterates, the generalized MEGNO is computed by means of

$$Y_{m,n}(N) = (m+1)\, N^n \sum_{k=1}^{N} \ln\left(\frac{\|\mathrm{v_k}\|}{\|\mathrm{v_{k-1}}\|}\right) k^m, \tag{10}$$

and

$$\overline{Y}_{m,n}(N) = \frac{1}{N^{m+n+1}} \sum_{k=1}^{N} Y_{m,n}(k)\,. \tag{11}$$

Further, a slight additional modification results profitable for the choice $(2, 0)$ of the exponents (m, n), which leads as to the quantity

$$\hat{Y}_{2,0}(N) = \left[4\overline{Y}_{2,0}(N) - 2\right]/N, \tag{12}$$

which tends to 0^- in the regular case and to σ_i, which is the LCN of the orbit, in the case of an irregular trajectory. Negative values of $\hat{Y}_{2,0}\,(N)$ appear for regular orbits –provided N is taken not too small–, while small positive values identify mild chaos.

5.2. The Coupled Rational Shifted Standard Map (CRSSM)

Let us introduce a 4D conservative map, namely, the Coupled Rational Shifted Standard Map (CRSSM) which provides a fairly good representation of the interaction of two perturbed resonances. Therefore, its dynamics would well serve to model many dynamical scenarios in astronomy and astrophysics.

The CRSSM is defined by:

$$\begin{aligned} y_1' &= y_1 + \varepsilon_1\, f_1(x_1) + \gamma_+\, f_3(x_1+x_2) + \gamma_-\, f_3(x_1-x_2),\\ y_2' &= y_2 + \varepsilon_2\, f_2(x_2) + \gamma_+\, f_3(x_1+x_2) - \gamma_-\, f_3(x_1-x_2),\\ x_1' &= x_1 + \varepsilon_1\, y_1',\\ x_2' &= x_2 + \varepsilon_2\, y_2', \end{aligned} \tag{13}$$

with $x_i \in [0, 2\pi)$, $y_i \in [0, 2\pi/\varepsilon_i)$, $i = 1, 2$, and

$$f_i(x) = \frac{\sin\,(x+\varphi_i)}{1-\mu_i\cos x} - \Delta_i, \qquad \Delta_i = \frac{\mu_i \sin\varphi_i}{\sqrt{1-\mu_i^2}+1-\mu_i^2}, \quad i = 1, 2, 3, \tag{14}$$

where $\mu_i \in [0, 1)$, and the quantities Δ_i are fixed so that the f_i functions have zero average.

Notice that (13) is a variation of two coupled standard maps so modified that symmetry is lost through the phase φ_i, and the entire character of f_i is broken due to the parameters $\mu_i \in [0, 1)$. The terms in $(x_1 + x_2)$ and $(x_1 - x_2)$ are coupled by the small terms including γ_+ and γ_- respectively. Thus defined, the map is a 4D–torus.

Though the CRSSM has too many free parameters most of them are kept fixed through all our study, being ε_2 the only one to be varied. We refer to CGS03 for the results concerning different sets of parameters.

Herein we fix $\mu_1 = 0.5$, $\varphi_1 = 1$, $\mu_2 = 0.4$, $\varphi_2 = 2$, $\mu_3 = 0.6$, $\varphi_3 = 3$, $\varepsilon_1 = 0.1$, $\gamma_+ = 0.1$, $\gamma_- = 0.05$ and take two distinct values of $\varepsilon_2 = 0.2, -0.2$.

5.3. Results provided by the MEGNO

For constructing Fig. 6, the MEGNO was computed for an equi-spaced grid of 1000×1000 pixels in the domain $(y_1\varepsilon_1/2\pi, y_2\varepsilon_2/2\pi) \in [0, 1) \times [0, 1)$, the initial values for the remaining variables being $x_1 = 0, x_2 = 0$. Recall that this is a problem of higher dimension, so that the iterates under DP of two "random" initial vectors $\mathrm{v}_{10}, \mathrm{v}_{20}$, satisfying $\|\mathrm{v}_{i0}\| = 1$, had to be computed - plus orthogonalized and renormalized at each step-, and the maximum of the two resulting values of $\hat{Y}_{2,0,\mathrm{RS}}$ –one associated to each direction– was taken to determine the character of each trajectory. The picture on the right corresponds to $\varepsilon_2 = 0.2$ and the one on the left to $\varepsilon_2 = -0.2$.

The contour–like plots exhibit the obtained values for $\log(\hat{Y}_{2,0,\mathrm{RS}})$ after $N = 10^4$ iterations, so that the details in each figure be highlighted. It is interesting

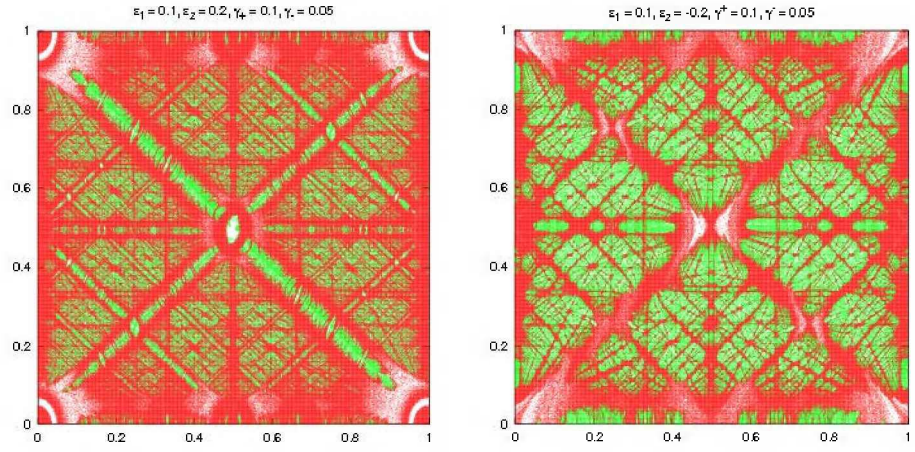

Figure 6. $\hat{Y}_{2,0,\mathrm{RS}}$–levels for the CRSSM on the (y_1, y_2)–plane taking values of ε_2 with opposite signs (0.2 at the left and -0.2 at the right) . Initial conditions of regular behavior are plotted in white, those of mild local instability in green while those exhibiting strong local instability in red.

to remark that in the coupling we face with an indefinite form rather than a positive definite one, which produces a pretty dramatic effect on the resonances. In fact, observe that in the case of positive ε_2 most of the resonances have an elliptical chain of tori at their center while for the negative value of such a parameter several resonances show up as totally hyperbolic. Note that we are dealing with an a priori unstable system (see for instance Lega *et. al*, 2010).

The resonances in the vertical and horizontal directions are present even if $\gamma_\pm = 0$ and their amplitudes depend, essentially, on ε_j, $j = 1, 2$. These resonances appear as white or green channels, despite of the sign of ε_2 and are the same present in the uncoupled Standard Map. Indeed, the sign of ε_i does not modify the uncoupled map, but it certainly affects the coupled one, since rescaling the y-variables, the CRSSM can be recast as

$$\begin{aligned} y_1' &= y_1 + \varepsilon_1^2 f_1(x_1) + \varepsilon_1\gamma_+ f_3(x_1 + x_2) + \varepsilon_1\gamma_- f_3(x_1 - x_2), \\ y_2' &= y_2 + \varepsilon_2^2 f_2(x_2) + \varepsilon_2\gamma_+ f_3(x_1 + x_2) - \varepsilon_2\gamma_- f_3(x_1 - x_2), \\ x_1' &= x_1 + y_1', \\ x_2' &= x_2 + y_2', \end{aligned} \tag{15}$$

where $(x_i, y_i) \in [0, 2\pi) \times [0, 2\pi)$.

Coupling the degrees of freedom, several new resonances arise, namely, those of the form $\alpha y_1 + \beta y_2 = \text{const.}$, with α and β non-vanishing constants. In fact, the map (15) can be derived from the 2.5 degrees of freedom Hamiltonian

$$\begin{aligned} H(p_1, p_2, x_1, x_2, t; \varepsilon_1, \varepsilon_2) &= H_0(p_1, p_2, x_1, x_2, t; \varepsilon_1, \varepsilon_2) + \gamma_+ V_p(x_1, x_2, t; \varepsilon_1, \varepsilon_2) \\ &+ \gamma_- V_n(x_1, x_2, t; \varepsilon_1, \varepsilon_2), \end{aligned} \tag{16}$$

where

$$H_0(p_1, p_2, x_1, x_2, t; \varepsilon_1, \varepsilon_2) = \frac{(p_1^2 + p_2^2)}{2} + \left(\varepsilon_1^2 U_1(x_1) + \varepsilon_2^2 U_2(x_2)\right) \delta_{2\pi}(t),$$

$$p_i = \frac{y_i}{2\pi}, \qquad f_i(x_i) = -\frac{1}{2\pi}\frac{dU_i}{dx_i}, \qquad i = 1, 2, \tag{17}$$

being $\delta_{2\pi}(t)$ the 2π–periodic delta defined through its Fourier expansion so that $t \bmod 2\pi$, and the coupling terms can be written as

$$\begin{aligned} V_p(x_1, x_2, t; \varepsilon_1, \varepsilon_2) &= (\varepsilon_1 + \varepsilon_2) U_3(x_1 + x_2)\delta_{2\pi}(t), \\ V_n(x_1, x_2, t; \varepsilon_1, \varepsilon_2) &= (\varepsilon_1 - \varepsilon_2) U_3(x_1 - x_2)\delta_{2\pi}(t). \end{aligned} \tag{18}$$

The relationship between f_3 and U_3 is similar to that defined above involving f_i and U_i for $i = 1, 2$. Since every function of t, x_1, x_2 id periodic, its Fourier expansion generates all kinds of resonances that, in action space, appear as straight lines as already mentioned. Indeed, the unperturbed frequencies, -that is when $\varepsilon_i = \gamma_i = 0$-, are $(\omega_1, \omega_2) = (y_1, y_2)$.

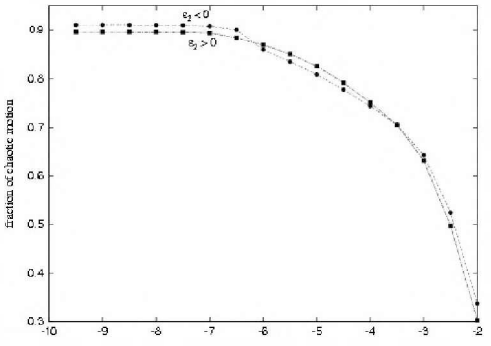

Figure 7. Fraction of chaotic motion in the maps corresponding to $\varepsilon_2 = 0.2$ and $\varepsilon_2 = -0.2$ against different threshold values of $\log(\hat{Y}_{2,0,\mathrm{RS}})$.

Let us now refer to Fig. 7 which displays the fraction of chaotic motion for the maps corresponding to the two opposite values of ε_2, for different thresholds of $\log(\hat{Y}_{2,0,\mathrm{RS}})$ below which global motion is regarded as regular. From this figure it could be deduced that $\log(\hat{Y}_{2,0,\mathrm{RS}}) \approx -6.5$ is a fairly adequate value to be adopted as a threshold in order to separate regular from chaotic dynamics. Notice that, for both values of ε_2, action space is almost completely chaotic – only about its 10% corresponding to regular motion– so it can be claimed that global chaos has set up in the system.

5.4. Diffusion on action space

With the aim of gaining some insight on the way diffusion operates, several orbits with initial conditions embedded in different chaotic domains were traced onto action space for both values of ε_2.

The wandering of the unperturbed integrals on the (y_1, y_2)–plane was pursued during 10^7 iterations for the initial conditions listed in Table 2, which, not only are located near the crossing of resonances, but have high values of the MEGNO, except for the initial conditions (iv) for $\varepsilon_2 = 0.2$ and (i) for $\varepsilon_2 = -0.2$, which correspond to stable motion.

As shown in Fig. 8 (corresponding to $\varepsilon_2 = 0.2$), the unperturbed integrals remain confined to rather small domains, so that diffusion turns out to be inefficient for a rather large number of iterates, as we observed in the case of the

Table 2. Initial conditions on action space in units of $2\pi/\varepsilon_j, j = 1,2$ (the same as in Fig.6) for five different orbits and its concomitant value of $\log(\hat{Y}_{2,0,\mathrm{rs}})$ for $\varepsilon_2 = 0.2$ (fourth column) and $\varepsilon_2 = -0.2$ (last column) after 10^4 iterations.

i.c.	y_1	y_2	$\log(\hat{Y}_{2,0,\mathrm{rs}})$	$\log(\hat{Y}_{2,0,\mathrm{rs}})$
			$\varepsilon_2 = 0.2$	$\varepsilon_2 = -0.2$
(i)	0.000	0.110	−2.435	−10.000
(ii)	0.000	0.500	−1.584	−1.436
(iii)	0.331	0.353	−1.712	−1.486
(iv)	0.500	0.500	−10.000	−1.449
(v)	0.074	0.336	−1.824	−1.794

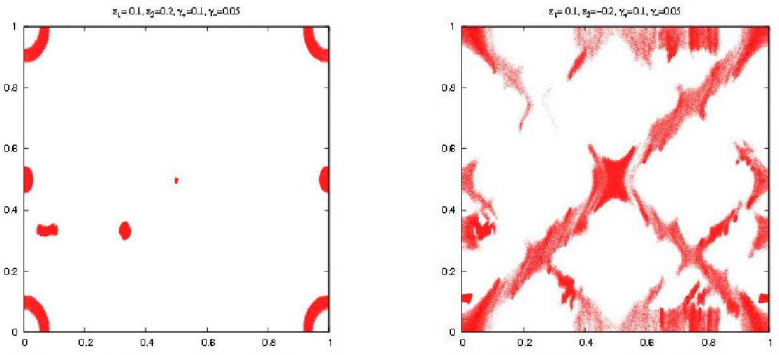

Figure 8. Diffusion on action space after 10^7 iterations of the map for the initial conditions listed in Table 2.

Hamiltonian system for the smaller perturbation parameter. This behaviour is usually referred to as stable chaos. Several papers due to Milani and co-workers (Milani & Nobili, 1992); (Milani, 1993); (Milani & Farinella, 1994); (Milani *et al.*, 1997) also address this topic. Moreover, further studies deal with the same phenomena of stable chaos (Morbidelli & Froeschlé 1995), which arises, for instance, in Solar System dynamics.

On the other hand, the plot in the panel corresponding to $\varepsilon_2 = -0.2$ exhibits the significant efficacy of the diffusive process (except for the initial condition (i) defining a stable orbit), and evinces that the relics of the unperturbed resonances serve as paths for diffusion. This mechanism is termed Arnol'd diffusion–like process and should not be confused with Arnol'd diffusion. In fact, this is what we have already observed in the case of the perturbed quartic oscillator for the largest value of the perturbation parameter. A detailed discussion about this issue and its departure from actual Arnol'd diffusion could be found in Giordano & Cincotta (2004); Cachucho *et al.* (2010) as well as in CGS03. Nonetheless, let us stress that the observed diffusion presents a geometrical resemblance with the Arnol'd theoretical conjecture according to which diffusion proceeds on phase space through the chaotic layers of the resonance web.

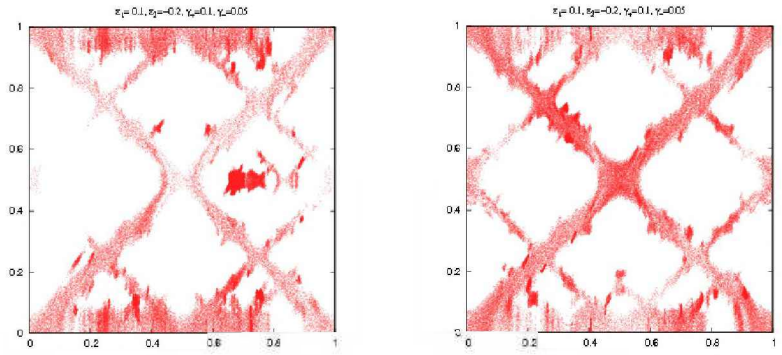

Figure 9. Diffusion on action space after 2×10^8 iterations of the map corresponding to $\varepsilon_2 = -0.2$ for i.c. (ii) in [a] and (iv) in [b].

Moreover, Fig. 9 illustrates that the orbits with initial conditions (ii) and (iv) for the case $\varepsilon_2 = -0.2$ sweep a rather large fraction of action space after 2×10^8 iterations. However, notice must be taken that the chaotic component of phase space is not fully connected for this timescale, since some chaotic domains remain unreached.

Fig. 10 depicts the time evolution of the initial condition (iv) after different iterations of the map in the case $\varepsilon = -0.2$. For 5×10^6 iterates the orbit remains confined to the central region while it spreads along some resonances for 10^8 iterates of the map. During the last 10^9 iterations the orbit explores several additional resonance remnants, though it is still far from visiting the entire chaotic component (compare with Fig. 6). Furthermore, for $N = 2 \times 10^9$, the trajectory seems to remain trapped in the horizontal resonance at $y_2 = 0.5$ (which has an elliptic structure) and no significant difference between the domains swept in the two last intervals of time is observed. These plots in fact could be considered as time-contour diagrams, since the more crowded regions should be associated to those domains of action space where the orbit spends more time.

5.5. A measure of diffusion

The classical approach for studying diffusive processes associated with the variation of any observable involves the analysis of the evolution of its mean square displacement. Certainly, the type of diffusion most studied is the normal one, mainly characterized by the linear scaling of the mean square displacement with time. Though, deviations from normal diffusion are frequently observed in many dynamical systems (see for instance Zhou *et al.* 2002; Cordeiro & Mendes de Souza 2005; Cordeiro 2006. This phenomena, termed anomalous diffusion in Metzler & Klafter (2000), affords also a characterization through the scaling of the variance (or the mean square displacement) with time but of a more general form.

Herein, we undergo the computation of a diffusion coefficient under the framework of normal diffusion in a rather simple fashion -following Chirikov (1979)-.

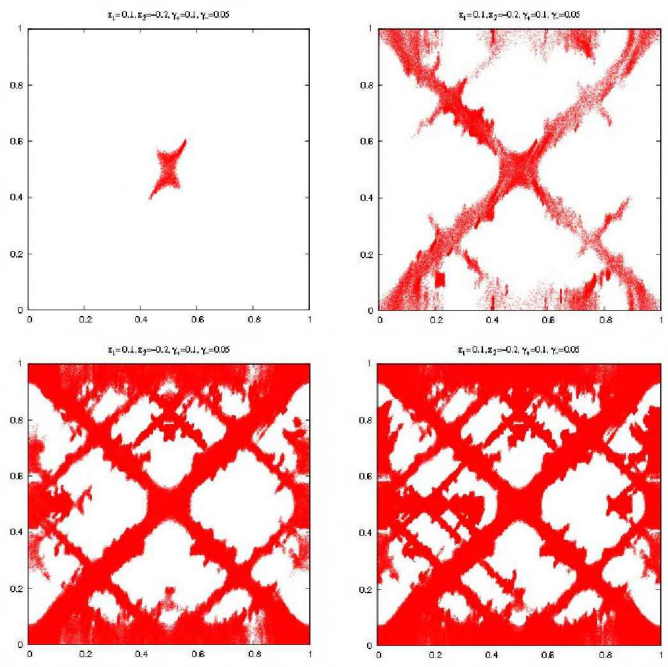

Figure 10. Diffusion after 5×10^6, 10^8, 10^9, 2×10^9 for a single orbit starting at the center for $\varepsilon = -0.2$.

Instead of tracing the evolution of a single orbit of the map, a diffusion coefficient for an ensemble of nearby orbits could be computed. To this end, and following the standard procedure in the case of random walk processes, let us define the finite time diffusion coefficient as the mean-square spread in y_i as (see Meiss, 1992)

$$\hat{D}_i = \frac{\mathrm{Var}[y_i]}{N}, \tag{19}$$

where $\mathrm{Var}[y_i]$ stands for the variance of the action and N for the entire time or number of iterates, so that the mean square span in each unperturbed action is given by

$$\sigma_i[y_i] = \sqrt{N\,\hat{D}_i}. \tag{20}$$

Finally, we introduce the quantity

$$D = \frac{\hat{D}_1 + \hat{D}_2}{2} \tag{21}$$

as a measure of the normal diffusion on the unperturbed actions–plane.

Recall that the map (13) is defined on a torus so, in order to avoid border effects that would artificially enlarge the value of the y_i–variance, the new variables

$$z_i = \cos(2\pi y_i), \qquad i = 1, 2. \tag{22}$$

are introduced, and the diffusion measure D is computed on the (z_1, z_2)–space instead of on the actual action space (y_1, y_2).

The roam of the unperturbed integrals onto the (y_1, y_2)–plane for five bundles around the initial conditions in Table 3 is depicted in Fig. 11, but, as already stated, it is the wandering onto the (z_1, z_2)–plane, shown in Fig. 12, the one to be used to compute the coefficient D defined by (21). For each one of these figures, an ensemble of 100 initial conditions chosen at random in a neighborhood of size 10^{-7} of conditions (i) to (v) were followed during 10^7 iterations of the map for both values of ε_2.

Furthermore, the averaged value of the diffusion for each ensemble was computed after 10^7 iterations. The concomitant out-coming values of D are displayed in Table 3.

Table 3. Initial conditions on action space in units of $2\pi/\varepsilon_j, j = 1, 2$ (the same as in Fig.6) for five different bundles of orbits and its concomitant value of $\log(D)$ for $\varepsilon_2 = 0.2$ (fourth column) and $\varepsilon_2 = -0.2$ (last column).

i.c.	y_1	y_2	$\log(D)$	$\log(D)$
			$\varepsilon_2 = 0.2$	$\varepsilon_2 = -0.2$
(i)	0.000	0.110	−8.666	−10.145
(ii)	0.000	0.500	−11.093	−7.438
(iii)	0.331	0.353	−9.027	−7.050
(iv)	0.500	0.500	−13.033	−7.993
(v)	0.074	0.336	−9.512	−8.034

Let us notice that the averaged values obtained for D fairly succeed in yielding a measure of the domain covered by the wandering of each bundle of initial conditions, displayed in Figs. 12.

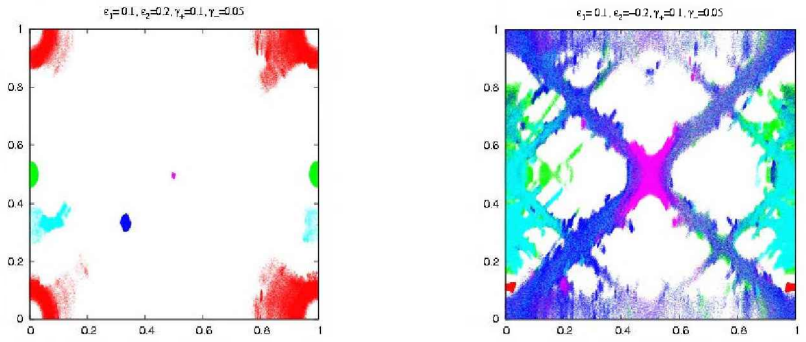

Figure 11. Diffusion on action space after 10^7 iterations of the map for the bundles of 100 initial conditions chosen at random around initial conditions listed in Table 3. Initial condition (*i*) in red, (*ii*) in green, (*iii*) in blue, (*iv*) in purple and (*v*) in light–blue.

In fact, for $\varepsilon = 0.2$ the lowest value of D corresponds to regular orbits at (iv), whose roam is practically restrained to a point being the motion essentially stable. For the remaining initial conditions, the out-coming value of D has the

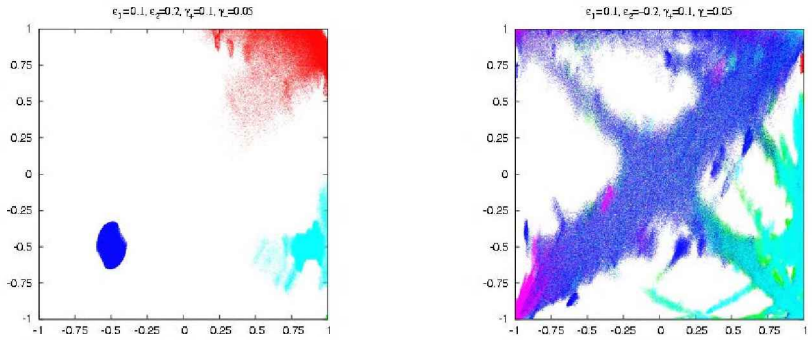

Figure 12. Diffusion on (z_1, z_2)–space after 10^7 iterations of the map for the bundles of 100 initial conditions chosen at random around initial conditions listed in Table 3, using the same color scheme.

same order of magnitude, the unperturbed integrals remaining confined to rather small domains of comparable extent for the number of iterates considered.

This fact can be confirmed when plotting the values of D for every orbit in each bundle as in Fig. 13, in which the last point in each curve corresponds to the averaged value for the ensemble.

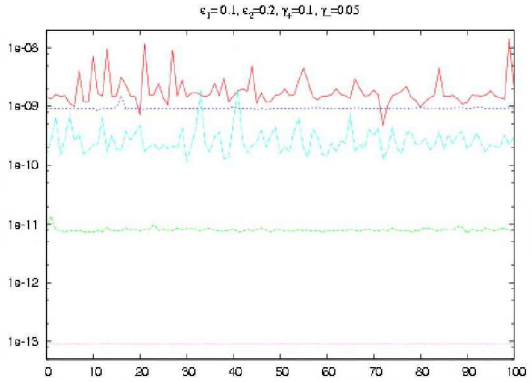

Figure 13. Diffusion measure on action space after 10^7 iterations of the map for $\varepsilon_2 = 0.2$ for a random selection of 100 initial conditions around (i) in red, (ii) in green, (iii) in blue, (iv) in purple, and (v) in light-blue.

The same procedure leads to Fig. 14 corresponding to $\varepsilon_2 = -0.2$. In particular this plot reveals the large dispersion in the values of D for each bundle, which gives account of the rather extended area swept by every bundle onto the (z_1, z_2)–plane.

Certainly, we could not invoke normal diffusion when dealing with systems of divided phase space. In fact, in such cases we ignore how the variance of the actions scale with time. Furthermore, though theories on abnormal diffusion and on sub–diffusion or super–diffusion have been developed, they seem to apply only for low dimensional systems.

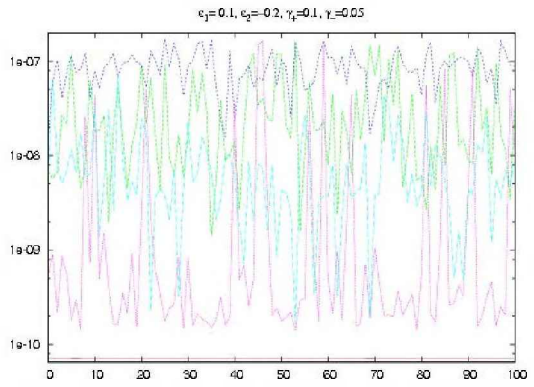

Figure 14. Diffusion measure on action space after 10^7 iterations of the map for $\varepsilon_2 = -0.2$ for a random selection of 100 initial conditions around (i) in red, (ii) in green, (iii) in blue, (iv) in purple, and (v) in light-blue.

Thus, the computation of a diffusion coefficient reveals itself as a cumbersome task. For instance, in Fig. 14 we observe fluctuations of three orders of magnitude in the 100 values of D within a domain of 10^{-7} around some of the chosen initial conditions.

Therefrom, in the forthcoming section we go beyond in the search of an alternative tool to measure diffusion bringing into play the finite time Shannon or Arnol'd Entropy.

5.6. The Shannon Entropy

Let us consider the time evolution of both normalized unperturbed actions $(y_1\varepsilon_1/2\pi, y_2\varepsilon_2/2\pi)$ upon the 2–torus T, or the unit square with opposite sides identified, as time goes by.

The evolution of the unperturbed integrals onto T is expected to be constrained to a small domain whenever a low diffusion takes place, while a large roam should be in order in case of fast diffusion.

An adequate tool to measure diffusion is the finite time *Shannon Entropy*. A theoretical background on Shannon Entropy can be found in e.g Shannon & Weaver (1949); Katz (1967); Arnol'd & Avez (1989); Wehrl (1978).

Thus, the main idea of the present approach is to make use of the Shannon Entropy -SE hereafter- in order to measure the wandering of the unperturbed action variables when viewed on the unit square.

Following Arnol'd & Avez (1989), let us recall the definition of the function Z over $[0, 1]$:

$$\begin{aligned} Z(x) &= -x\ln x, \quad x \in (0, 1] \\ Z(0) &= 0, \end{aligned}$$

which is continuous, nonnegative and strictly concave ($Z'' < 0$) and $Z(x) = 0$ corresponds to either $x = 0$ or $x = 1$.

Further, let $\alpha = \{a_i;\, i = 1, \cdots, q\}$ be a partition of T, that is to say, a collection of q boxes that cover the whole unit square. The boxes are assumed

to be both measurable and disjoint, that is to say

$$\mu\,(\,T\,-\,\cup_i a_i\,)\,=\,0,\qquad \mu\,(\,a_i\cap a_j\,)\,=\,0,\quad i\neq j,$$

where μ stands for a given measure.

We can define a probability density on T by

$$\varrho(\mathrm{x})\,=\,\frac{1}{N}\sum_{i=1}^{N}\delta(\mathrm{x}-\mathrm{x}_i), \tag{23}$$

where x_i denotes the result of a given iterate on T, and δ is the *delta function.* It can be verified at once that

$$\int_T \varrho(\mathrm{x})\;\,d\mathrm{x}\,=\,1, \tag{24}$$

and the probability of the element a_i of the partition turns out to be

$$\mu(a_i)\,=\,\int_{a_i}\varrho(\mathrm{x})\;\,d\mathrm{x}. \tag{25}$$

Finally, the entropy of the partition α is defined as

$$S(\alpha)\,=\,\sum_{i=1}^{q} Z\,(\,\mu(a_i)\,)\,=\,-\sum_{i=1}^{q}\mu(a_i)\ln(\mu(a_i)). \tag{26}$$

Let us notice that for a given partition α, the entropy is a bounded quantity. In fact, it is $0\,\leq\,S(\alpha)\,\leq\,\ln q$. The minimum value is reached when all points fall in the very same element of the partition, say the k–th element, which would correspond to the case of almost full stability (for instance when all the iterates lead to the same action value). Indeed, in such a case, we have a unique nonzero value $\mu(a_k)\,=\,1$, yielding $S\,=\,0$. On the other hand, the maximum value, $S(\alpha)\,=\,\ln q$, will be reached whenever the q elements of the partition have equal measure $\mu(a_i)\,=\,1/q$, that corresponds to the situation in which the unperturbed actions wander all over the unit square in a uniform fashion, i.e. in case of ergodicity.

Hereafter, S will denote the normalized value of the entropy (i.e. the entropy divided by $\ln q$) for a given partition α.

Note that if we assume all the non-empty elements of the partition, say q_0, having the same measure, then $S\,\approx\,\ln q_0/\ln q$.

Let us now accomplish the computation of the finite time SE for a given set of initial conditions for the CRSSM (13) with the same set of parameters.

To this end, we take a partition of $q\,=\,m\times m$ bidimensional boxes that cover the whole unit square, for an equi–spaced grid of $1000\,\times\,1000$ initial conditions in the domain $(y_1\varepsilon_1/2\pi, y_2\varepsilon_2/2\pi)\,\in\,[0,1)\,\times\,[0,1)$. The initial values for the remaining variables are $x_1\,=\,0, x_2\,=\,0$, and we consider $N\,=\,10^7$.

Let us say that we have defined the partition in regards to the total number of iterates such that in case of a uniform distribution the same number of points

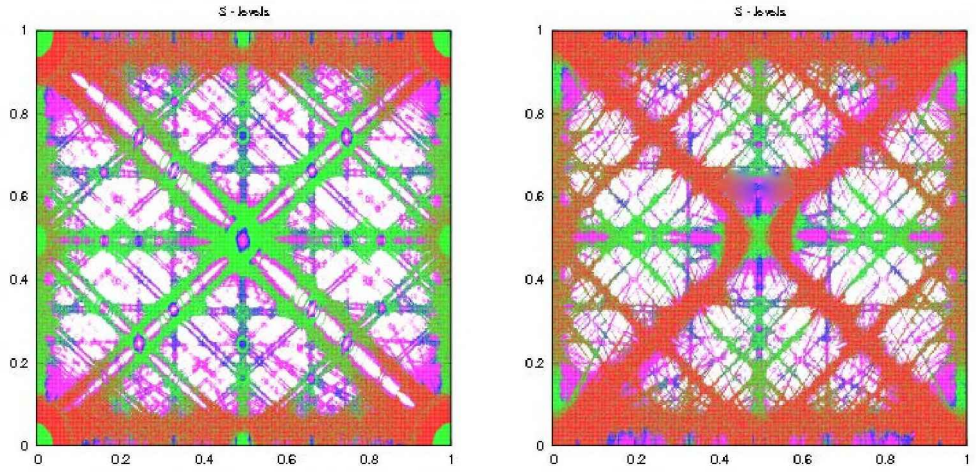

Figure 15. S–levels for the CRSSM on the (y_1, y_2)–plane after $N = 10^7$ iterates of the map for a grid of 1000×1000 initial conditions of the unperturbed actions for ε_2 with opposite signs. Values of $S < 0.38$ are depicted in white, $0.38 \leq S < 0.45$ in purple, $0.45 \leq S < 0.5$ in blue, $0.5 \leq S < 0.66$ in green and $0.66 \leq S$ in red. In terms of the number of visited elements of the partition, q_0, the intervals correspond to $q_0 < 2 \times 10^2$ in white, $2 \times 10^2 \leq q_0 < 5 \times 10^2$ in purple, $5 \times 10^2 \leq q_0 < 10^3$ in blue, $10^3 \leq q_0 < 10^4$ in green and $10^4 \leq q_0$ in red.

would lie in each individual cell. The results are given in Fig. 15, the plot on the left corresponding to $\varepsilon = 0.2$ and that on the right to $\varepsilon = -0.2$.

Let us remark that the results obtained by means of the SE are also in quite good agreement with those obtained by recourse to the MEGNO, except in those regions of slow or fast diffusion.

Let us note that the resonance structure arising in the contour–plots obtained with the SE resembles the one revealed by the MEGNO. Moreover, the effect on the resonances due to the change of sign of ε_2 remains noticeable. Indeed, as already pointed out, in the case of positive ε_2 most of the resonances display an elliptical chain of tori at their center while for negative ε_2 several resonances show up as totally hyperbolic. However, while the MEGNO just measures the local hyperbolicity of a certain point in phase space, the SE provides information about chaotic diffusion in such a point. This can be clearly seen, for instance in the case for $\varepsilon_2 = -0.2$, by the small values adopted by the SE along the resonance at $y_2 = 0.5$, whose structure seems to act as a barrier to diffusion as we have already shown.

Although the SE depends on the partition, in our experiments no significant differences have been observed when using different α's.

While for $N \to \infty$ the SE (in phase space) should become the metric entropy -which is related to the sum of the positive Lyapunov's exponents- this seems not to be the case for any finite, though very large, number of iterates N.

6. Theoretical considerations, observational constraints and open problems

In this section we summarize some theoretical considerations, observational data and results from N–body simulations and finally some open questions.

6.1. Theoretical considerations

- The overlap of resonances (heteroclinic intersections) and Arnol'd diffusion–like processes are well–known mechanisms that lead to the transition from regularity to gross chaos (or gross instabilities).
- We claim that "classical" Arnol'd diffusion does not play any role in galactic dynamics (even in asteroidal dynamics), since in general "the perturbation" is not small enough, and even if it might work, its timescale is quite large for any real system, as shown in our simple experiments. We do not believe that Arnol'd diffusion could describe global instabilities.
- Though one could get accurate values of any indicator of the stability of the motion, they only provide the local rate of exponential divergence and this is not related to any global instability.
- Chaos or global instabilities should be understood as large variations of the unperturbed integrals (diffusion). Unfortunately, as far as we know, it does not yet exist any theory that could describe global diffusion (instability) in phase space.
- However what it is actually relevant is the extent of the domain upon which the unperturbed integrals change and, physically, the timescale in which this diffusion occur.
- Those timescales for galaxies which are less or similar than the Hubble time $T_H \sim 10^3 T_c$,, being T_c the characteristic timescale for a given galaxy, seem to be too short in order to any kind of global diffusion be efficient. Perhaps in some cases, the overlap of resonances, whose rate is $\sim$ some power of the perturbation parameter could lead to some diffusion, connecting nearby regions of phase space.
- Arnol'd diffusion, or to be more precise, Arnol'd mechanism, only states that two points of phase space separated by a distance of $\boldsymbol{O}(1)$ could be connected. This result does not imply any global instability and, in fact, just for this case it requires exponentially large times. Thus, we believe that Arnol'd diffusion does not play any role in galactic dynamics.
- Arnol'd diffusion–like processes perhaps also could not operate in galactic dynamics, as we have already shown. It might be a plausible mechanism in asteroidal dynamics though.

6.2. Observational data and N–body simulations

- Observations with the HST revealed the presence of very high stellar densities at the center of early-type galaxies, which suggest that rhey could

be fitted by a power law of the form ($r^{-\gamma}$). The evidence of large central masses was also reinforced from high-resolution kinematical studies of nuclear stars and gas, which disclosed the presence of compact dark objects with masses in the range of $10^{6.5} - 10^{9.5} M_{\odot}$, presumably super–massive black holes. These observational results have produced a substantial change in the classic ideas on dynamics in triaxial galaxies.

- Numerical simulations show that the addition of a central mass to an integrable triaxial potential has deep effects on its dynamics, at least for the boxlike orbits which mainly cover the central region of triaxial galaxies.

- Black holes and central density cusps scatter these particular orbits during each close passage giving rise to chaos in the system. The sensitivity of boxlike orbits to deflexions also drives a rounder central distribution of mass. This slow evolution towards axisymmetry suggests that stationary triaxial configurations could not exist for a strong central density cusp.

- For such large values of M_{bh}, the box orbit phase space is almost completely stochastic since overlap of resonances and diffusive processes could take place in rather short timescales.

- This result turned out to be substantially attractive because this critical black hole mass was close to the one observed and also close to the mass which induced a sudden evolution towards the axisymmetry in N–body simulations.

- Merritt & Fridman (1996) arrived to similar conclusions analyzing two triaxial power law models $r^{-\gamma}$: the steep ($\gamma = 2$) and the weak ($\gamma = 1$) cusp. They found, in agreement with Gerhard & Binney (1985), that triaxial galaxies with such a huge concentration of mass would evolve towards a central axisymmetry, as box orbits loose their distinguishability.

- For these models, in which a large fraction of phase space is dominated by a chaotic dynamics, the construction of self-consistent solutions requires the inclusion of stochastic orbits besides the regular ones. A system thus built evolves, mainly close to its center, as stochastic orbits mix through phase space.

- Though it is possible to build this kind of solutions for a weak cusp model, this is not the case for a strongly concentrated model. This would imply that triaxility is not consistent with a high central density.

- How could the correlation between the velocity dispersion and the black holes masses be explained?

6.3. Open problems

- Nature's ability to build stationary non–axisymetric stellar systems is still en open matter.

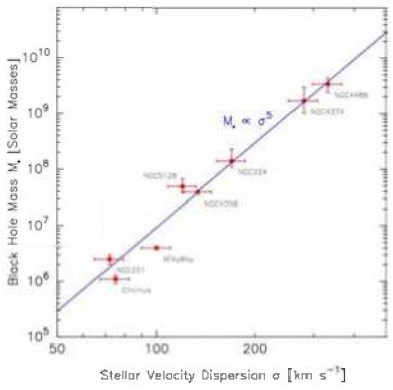

Figure 16. Correlation between the velocity dispersion and the mass of the (assumed) black hole in different galaxies. (This figure was generously provided by D. Merritt).

- Merritt's generalization of Jeans Theorem rests on a very strong assumption: a completely connected chaotic component must exist in a 3D system with divided phase space. It seems that this could happen only whether the chaotic component has a large measure and "$t \to \infty$", which, from a physical point of view, it would not be possible in galactic systems, where the chaotic component has a small measure and $t \lesssim T_H$.

- An important fact to be stated is that when chaos sets up, the unperturbed global integrals (or actions) have a discontinuous dependence on phase space variables. Indeed, close to resonant tori, despite the existence of three local integrals, the unperturbed orbital structure is not preserved and the topology of phase space changes. Moreover, at least one integral does not exist on the stochastic layer.

- Close to strong non–resonant tori, those satisfying the Diophantine condition, local integrals are just corrections of order ε of the unperturbed global integrals. On the other hand, when the system is close to an elliptic resonant torus, new local integrals appear: the pendulum Hamiltonian H_r and linear combinations, K_2, K_3, of the unperturbed actions at the resonant point.

- It is not possible to assume that the DF has the form $f(H, I_2, I_3)$ in the whole regular component. This could be true only for strong non–resonant tori, but since resonances are dense in phase space, the DF should be locally defined as: $f_n(H, I_2, I_3)+\varepsilon g(H, I_2, I_3)$ in a neighborhood of a non–resonant torus and $f_r(H_r, K_2, K_3)$ in a vicinity of an elliptical resonant torus.

- Is the distribution function of the galaxy best fitted by a two–(local)integral or three-(local)integral model?

- Nothing could be said about f in the chaotic domain since there is no theoretical support to argue that the whole chaotic region is fully connected. Clearly, a notorious discontinuous dependence of f on the integrals is expected.

- Does the introduction of a black hole ("singularity") at the origin change the approach to the problem? Indeed, if we perform a multipolar expansion of the potential for an elliptical galaxy, the introduction of a mass point perturbation would drastically modify the unperturbed part of the Hamiltonian: that corresponding to the monopole term.

- How should diffusion be measured? It seems natural to think that it is related with the variance of the integrals. But in which way?

- How should the existence of barriers and "accelerators" of diffusion be included in the computation of the coefficient?

- And finally, how could diffusion routes be predicted?

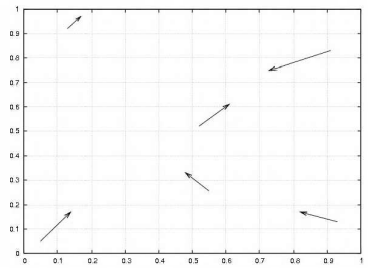

Figure 17. The length of the arrows would measure the rate of diffusion at that point in phase space and their direction points out its route after some time interval.

Acknowledgments. This work was supported with grants from the *Consejo de Investigaciones Científicas y Técnicas de la República Argentina*, and the *Universidad Nacional de La Plata.*

References

Arnol'd, V. I., 1964, Sov. Math.-Dokl. 5, p. 581.

Arnol'd, V. & Avez, A., 1989, Ergodic Problems of Classical Mechanics, 2nd. Ed. (Addison-Wesley, New York).

Binney, J. & Tremaine, S., 1987, Galactic Dynamics, (Princeton University Press: New Jersey).

Cachucho, F., Cincotta, P., Ferraz–Mello, S., 2010, CMDA, 108, 35.

Carati, A & Galgani, L., 2012, Proc. of the Third La Plata School on Astronomy and Geophysics, Cincotta, P., Giordano, C., & Efthymiopoulos, C. (eds.), (La Plata), this volume.

Chirikov, B.V., 1979, Physics Reports 52, 263.

Chirikov, B., Lieberman, M., Shepelyansky, D., Vivaldi, F., 1985, Physica D, 14, 289.

Chirikov, B. & Vecheslavov, V., 1989, Preprint INP, 89, Novosibirsk.

Chirikov, B. & Vecheslavov, V., 1993, J. Stat. Phys. 71, 243.

Cincotta, P.M. & Simó, C., 2000, A&A, 147, 205.

Cincotta, P.M., 2002, New Astronomy Reviews, 46, 13.

Cincotta, P.M. & Giordano, C.M., 2002, Proc. Advances in Space Dynamics 2. Applications in Astronomy, Winter O., Prado A.F.B.A, (eds.), (I.N.P.E., São Paulo), 237.

Cincotta, P.M., Giordano, C.M. & Simó, C., 2003, Physica D, 182, 151 (CGS03).

Cincotta, P.M. & Giordano, C.M. 2008, New Nonlinear Phenomena Research, (New York: Nova Science Pub. Inc., Perlidze T. ed.), Ch. 6, 393.

Cincotta, P.M. & Giordano, C.M., 2012, IJBC, in press.

Cordeiro, R. & Mendes de Souza, L., 2005, AJ, 439, 375.

Cordeiro, R., 2006, AJ, 132, 2114.

Efthymiopoulos, C., Voglis, N. & Kalapotharakos. C., 2007, LNP, 729, 297.

Efthymiopoulos, C., 2012, Proc. of the Third La Plata School on Astronomy and Geophysics, Cincotta, P., Giordano, C., & Efthymiopoulos, C. (eds.), (La Plata), this volume.

Froeschlé, C., 1971, Astrophys. Space Sci. 15, 110.

Froeschlé, C., 1972, å, 16, 172.

Froeschlé, C., Guzzo, M. & Lega, E., 2005, CMDA, 92, 243.

Gerhard, O.E. & Binney, J.J., 1985, MNRAS, 216, 467.

Giordano, C. M. & Cincotta, P., 2004, A&A, 423, 745.

Guzzo, M., Lega E. & Froeschlé, C., 2002, Physica D, 163, 1.

Guzzo, M., Lega, E., & Froeschlé, C., 2005, DCDS B 5, 687.

Guzzo, M., Lega, E. & Froesché, C., 2006, Nonlinearity, 19, 1049.

Katz, A., 1967, Principles of Statistical Mechanics, The Information Theory Approach, (San Francisco: W.H. Freeman & Co.).

Hairer, E., Norsett, S. & Wanner, G., 1987, Solving Ordinary Differential Equations. I. Nonstiff Problems, (Springer: New York).

Korabel, N. & Klages, R., 2004, Physica D, 187, 66.

Lega, E., Froeschlé, C. & Guzzo, M., 2008, LNP, 729, 29.

Lega, E., Guzzo, M. & Froeschlé, C., 2010, CMDA, 107, 115.

Lochak, P., 1999, Proc. Hamiltonian Systems with Three or More Degrees of Freedom', Simó C. (ed.), (Kluwer, Dordrecht), 168.

Lynden-Bell, D., 1962, MNRAS, 124, 1.

Mestre, M., 2012. Difusión Caótica de Sistemas Hamiltonianos casi–integrables, Ph.D Thesis. Universidad Nacional de La Plata.

Merritt D. & Friedman T., 1996, ApJ, 460, 136.

Merritt D. & Valluri M., 1996, ApJ, 471, 82.

Merritt, D., 1999, PASP, 111, 129.

Meiss, J., 1992, Rev. Mod. Phys. 64, 795.

Mestre, M, Cincotta, P. & Giordano, C., 2009. IJNLM, 44, 179.

Metzler, R. & Klafter, J., 2000, Physics Reports, 339, 1.

Milani, A. & Nobili, A. M., 1992, Nat, 357, 569.

Milani, A., 1993, CMDA, 57, 59.

Milani, A. & Farinella, P., 1994, Nat, 370, 40.

Milani, A., Nobili, A. M. & Knezevic, Z., 1997, Icarus, 125, 13.

Morbidelli, A. & Froeschlé, C., 1996, CMDA, 63, 227.

Muzzio, J.C., Carpintero, D.D., & Wachlin, F.C., 2005, CMDA, 91, 173.

Papaphilippou Y. & Laskar J., 1998, A&A, 329, 451.

Poincaré, H., 1893, Les Méthodes Nouvelles de la Mécanique Céleste, (Gautier–Villars: Paris).

Poon, M. & Merritt, D., 2002, ApJ, 568, 89.

Shannon, C. & Weaver, W., 1949, The Mathematical Theory of Communication, (Urbana: Illinois U.P.).

Venegeroles, 2008, Phys. Rev. Lett., 101, 54102.

Wehrl, A., 1978, Rev. Mod. Phys., 50, 221.

Zhou, J., Sun, Y. & Zhou L., 2002, CMDA 84, 409.